JMEPEG (2024) 33:7265–7276
https://doi.org/10.1007/s11665-023-08444-w

1059-9495/$19.00

ORIGINAL RESEARCH ARTICLE

The Effect of Ti Doping on the Thermoelectric Performance of Bi_2Te_3 and Its Chemical Stability

Mohammad Dani Al Qori', Nadya Larasati Kartika, Asep Ridwan Nugraha, Bintang Surya Bhakti, Ahmad Riziq Mubarok, Asep Rusmana, Ardita Septiani, and Dedi

Submitted: 9 March 2023 / Revised: 1 June 2023 / Accepted: 11 June 2023 / Published online: 12 July 2023

Bismuth telluride and its alloys are widely used as materials for thermoelectric generators (TEGs) with excellent performance at room temperature. In this research, we synthesized $Bi_{(2-x)}Ti_xTe_3$-doped variants (x = 0, 0.05, 0.1, and 0.15) by using a solid-state reaction and carbon burial sintering method. Powder x-ray diffraction (XRD) showed that the cell structure formed was rhombohedral with a space group of $R\bar{3}m$. Rietveld refinement revealed that the cell volume decreased with increasing dopant amount because Ti^{4+} has a smaller radius than Bi^{3+}. Ti doping widened the energy gap and decreased the concentration of charge carriers, which increased resistivity. The undoped sample had the highest figure of merit (zT) relative to doped samples, which was 0.46 at a temperature of 327 K. However, Ti doping in the Bi_2Te_3 system reduced the corrosion rate and increased hardness.

Keywords cell volume, corrosion rate, figure of merit, hardness, Ti doping

1. Introduction

Thermoelectric generators (TEGs) have been the subject of many studies since TEGs provide increased efficiency. TEGs convert thermal energy into electrical energy directly or vice versa (Ref 1). Many researchers have investigated issues related to the efficiency of thermoelectric materials. The power factor (PF) is one of the variables indicating the performance of the TEGs, which is obtained from measurements of the Seebeck coefficient (S) and electrical resistivity (ρ). Mathematically, this can be written as

$$\mathrm{PF} = \frac{S^2}{\rho} \qquad \text{(Eq 1)}$$

In addition, a variable to calculate performance that takes into account thermal conductivity (κ) is the figure of merit (zT). The equation is written as follows:

$$\mathrm{zT} = \left(\frac{\mathrm{S}^2\sigma}{\kappa_\mathrm{e} + \kappa_\mathrm{l}}\mathrm{T}\right) \qquad \text{(Eq 2)}$$

which is dimensionless (Ref 2). According to the equation, to obtain a large zT value, a high S, high σ, and low κ are needed.

Mohammad Dani Al Qori', Nadya Larasati Kartika, Asep Ridwan Nugraha, Asep Rusmana, Ardita Septiani, and **Dedi**, Research Centre for Advanced Materials, National Research and Innovation Agency, South Tangerang 15314 Banten, Indonesia; **Bintang Surya Bhakti** and **Ahmad Riziq Mubarok**, Department of Metallurgy, Universitas Jenderal Achmad Yani (UNJANI), Faculty of Manufacturing Technology, Bandung 40285, Indonesia. Contact e-mails: dedi011@brin.go.id and dediamada1@gmail.com.

There are several techniques to increase the value of zT, one of which is forming nanopores in nanoplates. Nanoscale pores can reduce thermal conductivity but do not affect electrical conductivity (Ref 3, 4). The figure of merit equation shows that the thermal conductivity mechanism is influenced by two variables, the effect of charge carriers (κ_e) and phonons (κ_l). For materials that have high σ, the κ value is dominated by the contribution of electrons. Therefore, the zT value depends heavily on S. Wiedemann–Franz's law explains that the value of κ_e can be calculated by knowing the σ value, the measurement temperature (T), and the Lorenz number (L) as shown in the following equation:

$$\kappa_e = L\sigma T \qquad \text{(Eq 3)}$$

For free electrons, L is equal to 2.44×10^{-8} WΩK^{-2}. Kim *et al* proposed a single parabolic band (SPB) model to calculate the L value, which depends on the value of S (Ref 5). Many thermoelectric materials are being explored for power generation applications, such as Sb_2Te_3 (Ref 6), Ag_2Te (Ref 6), Bi_2Te_3 (Ref 7), PbTe (Ref 8, 9), GeTe (Ref 10–12), SnTe (Ref 13) and MnSi (Ref 14). However, Bi_2Te_3 is the most popular thermoelectric (TE) material, and it shows excellent performance at room temperature (Ref 15). Bi_2Te_3 has a rhombohedral unit cell with a space group of $R\bar{3}m$, where the unit cell is located in a hexagonal close-packed (HCP) structure. In a unit cell, there are two Bi and three Te atoms. The HCP structure consists of quintuple layers (Te_2-Bi-Te_1-Bi-Te_2) in which van der Waals bonding exists between each layer. The Te_2-Te_2 bond is weak and is easy to cleave. The nature of the bonding between Bi and Te in the layer is ionic-covalent (Ref 16). At room temperature, the lattice parameters are $a = b = 4.3866(2)$ Å and $c = 30.4978(13)$ Å (Ref 17). Bi_2Te_3 has a narrow energy gap. The calculations carried out by Lawal *et al*. with and without spin-orbit coupling show that the energy gaps are 0.13 eV and 0.31 eV, respectively (Ref 18). There are several methods used to synthesize Bi_2Te_3-based materials, including hydrothermal (Ref 19), coprecipitation (Ref 20), solid-state reaction (Ref 21), and sol–gel (Ref 22) methods. However, the solid-state reaction is the simplest method to carry out. Several previous reports have shown that to improve the performance of thermoelectric properties, doping or compositing can be performed with other elements or compounds. Mg (Ref 23), Lu (Ref 24, 25), Dy (Ref 26), Ce (Ref 27), Tm (Ref 24), Se (Ref 28), Cu (Ref 29), Sn and CuI (Ref 7) doped or composited with CNTs can increase the S value and decrease the κ value of the material (Ref 30). Previously, research was carried out by Kartika et al. on the effect of Ti doping on the Bi_2Te_3 system. It was based on research conducted by Drašar et al., who performed Ti doping on Sb_2Te_3. Because Sb_2Te_3 has a similar structure, it is also possible to dope Ti into Bi_2Te_3. Interestingly, the hardness value tends to increase with the concentration of dopant compared to the pristine material (Ref 31, 32). In this research, Ti doping was carried out in the Bi_2Te_3 system particularly to study changes in the figure of merit (zT) as a result of doping, which has not been investigated in previous research.

2. Experiment

$Bi_{(2-x)}Ti_xTe_3$ with various dopant amounts (x = 0, 0.05, 0.1, and 0.15) was synthesized using a solid-state reaction method. The precursors used were Bi powder (95.5% purity, Polamet), Ti powder (≥ 98% purity, Merck), and Te powder (99.8% purity, Sigma–Aldrich). All precursors were mixed by grinding in an agate mortar for 1 hour according to the stoichiometry of the doping variants. The powders were compressed at 60 MPa on a 12-mm-diameter steel die. The pellets were buried in carbon powder in an alumina crucible with a lid to prevent oxidation during the heating process. Sintering was performed with the carbon burial method as described in previous research (Ref 26, 32, 33). Sintering was carried out at a temperature of 480 °C for 6 hours and a heating rate of 300 °C/h. The crystal structure was analyzed by powder x-ray diffraction (XRD, Bruker, D8 Advanced) and Bragg–Brentano diffraction at 40 kV and 40 mA with Cu-kα radiation at ~ 1.5406 Å. Measurements were conducted at room temperature in the range of 10-90° with a step size of 0.020°. First, the XRD data were analyzed qualitatively; that is, each peak was matched with databases from PDF 01-083-5983. Quantitative analysis was carried out using the Rietveld method with the *GSAS-II* program (Ref 34). Scanning electron microscopy (SEM, Jeol JSM-IT300) and energy-dispersive x-ray spectroscopy (EDS, Oxford Xmax 30) were used to observe the size and morphology of the particles and the ratio between constituent elements. The Seebeck coefficient (S) and resistivity (ρ) were measured using an LSR-4 (Linseis, Germany) in a helium atmosphere at a low pressure of 0.2 bar. Resistivity was measured using a four-point probe configuration with a distance between voltage probes of 6 mm. The applied current was 100 mA. All bulk samples were measured at a temperature range of 323-463 K at a temperature interval of 20 °C. The figure of merit (zT) could be directly determined using the Harman method on the same instrument. In principle, the Seebeck voltage is divided by the Ohmic voltage (Ref 35). Ni and Ni-Cr alloy wires were attached to the samples as voltage probes using a Hotspot TC Welder. The samples responded to the voltage of the applied current, which was 40 and 50 mA, and the acquisition times were 275 and 300 s, respectively. Hardness measurements were performed by using a Micro Vickers hardness tester in five different areas. The mass load was 25 gr, and the loading time was 10 s. The energy gap was characterized by using UV–Vis spectrophotometry (SPECORD 210 PLUS) in the wavelength range of 185-1100 nm. The corrosion rates were measured using a potentiodynamic corrosion tester in NaCl electrolyte solution with a mass fraction of 3% (Ref 36). The electronic structure of Bi_2Te_3 was calculated in Quantum Espresso version 6 using the density functional theory method (Ref 37, 38). The band structure, density of states, and partial density of states calculations of the relaxed structure of bismuth-telluride were performed using generalized gradient approximation (GGA) based on Perdew–Burke–Ernzerhof revised for solids (PBEsol) (Ref 39, 40). The partial density of states was applied to determine the density of states of each atom in the unit cell structure. The projected augmented wave (PAW) and ultrasoft pseudopotential were used without and with spin-orbit coupling, respectively, in the self-consistent field (SCF) calculation (Ref 41, 42).

3. Results and Discussion

Figure 1(a) shows the powder XRD pattern of $Bi_{(2-x)}Ti_xTe_3$ for a range of doping levels. The main phase of Bi_2Te_3 is formed, while there are peaks of the impurity phase of Bi_2TeO_5 (COD 4319514), which is marked with a star. The presence of Bi_2TeO_5 might be caused by oxidation during the sintering process, in which the particles on the Bi_2Te_3 surface absorb oxygen (Ref 43). Ti substitutes for sites with Bi due to their similarity in oxidation number and ionic radii. It can be seen from the highest peak in the XRD data, as shown in Fig. 1(b), that increasing the Ti doping concentration causes a shift in the peak (10-5) toward a higher angle. According to Bragg's law, the shift is due to a reduction in the size of the lattice volume because the ionic radius of Ti^{4+} is smaller than that of Bi^{3+}, at

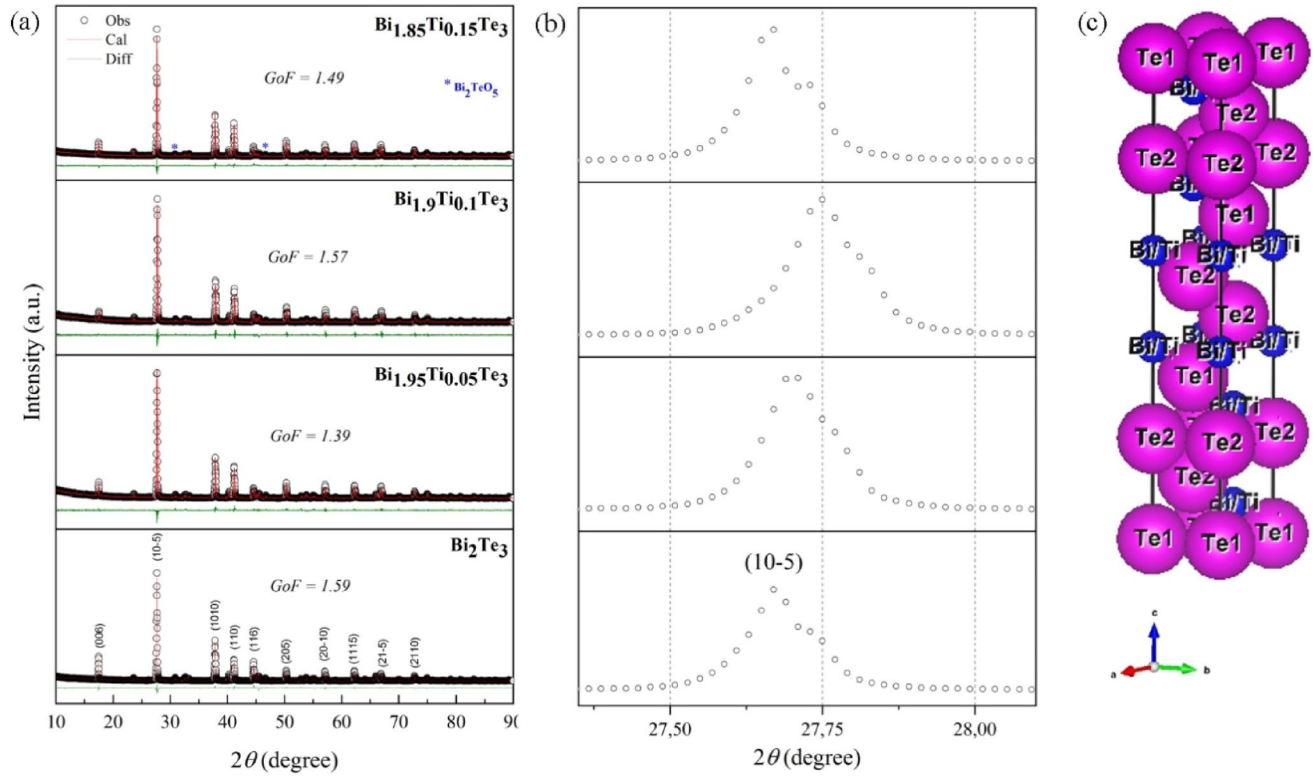

Fig. 1 (a) XRD pattern of several samples of $Bi_{(2-x)}Ti_xTe_3$ in doped variants (x = 0.0, 0.05, 0.1, 0.15). The main phase was defined by a rhombohedral crystal structure with a space group of $R\,\overline{3}\,m$ (PDF 01-083-5983), while for the impurity phase, an orthorhombic crystal structure with a space group of *Abm*2 (COD 4319514) was used. (b) Peak shift (10-5) at 2θ = 27.5-28° as influenced by Ti doping. (c) Crystal structure of $Bi_{1.95}Ti_{0.05}Te_3$

0.745 Å and 1.17 Å, respectively (Ref 44, 45). The peak shift is not linear at the highest doping level. The shift in the peak toward a lower angle at doping level $x = 0.15$ potentially occurs because not all Ti atoms can occupy the atomic positions of Bi. This analysis is based on the results reported by Kartika et al., who mixed Ti with a Bi_2Te_3 compound and showed a shift in the peak toward a lower angle as a function of increasing Ti concentration (Ref 32). Based on the results of this research shown in Table 1, the lattice volume decreased as a function of doping but not for the highest doping level. The increasing cell volume at the $x = 0.15$ doping level is hypothesized to be due to the presence of independent Ti. An increase in the volume of Bi_2Te_3 cells was also reported by Kulsi et al. when it was composited with RGO (Ref 46). Nonlinear changes at high doping concentrations also apply to local structures, distances, and angle bonding. Crystallite size and lattice strain can be analyzed by using the Williamson-Hall model.

$$\beta \cos\theta = \frac{K\lambda}{D} + \varepsilon(4\sin\theta) \qquad \text{(Eq 4)}$$

where β is the FWHM (full width at half maximum), K is the form factor, λ is the wavelength of Cu-kα radiation, and D is the crystallite size (Ref 47, 48).

Figure 2(a-e) gives some information about the surface morphology and EDS measurement results of $Bi_{(2-X)}Ti_XTe_3$ samples. Grain boundaries are shown on the order of μm. The experimental results of all samples show that the ratio between Te and Bi is slightly below that from theoretical calculations. Therefore, it can be concluded that Te is deficient in all samples. EDS also exhibited the elemental spectrum of oxygen, which confirmed that the XRD pattern indicated a peak for the Bi_2TeO_5 phase. Ti was detected only in the sample with the

Table 1 Lattice parameters, phase fraction, cell volume, local structure (distance and angle of bonding), atomic position of Bi, Te, and Ti as a result of refinement using the rhombohedral crystal with a space group of *R* −3 *m* as well as crystallite size and lattice strain obtained from analysis using the Williamson-Hall model on all samples as influenced by Ti doping

Phase	Bi_2Te_3	$Bi_{1.95}Ti_{0.05}Te_3$	$Bi_{1.9}Ti_{0.1}Te_3$	$Bi_{1.85}Ti_{0.15}Te_3$
Lattice Parameters, Å	$a = b = 4.3872(3)$*; $c = 30.4967(3)$	$a = b = 4.3867(6)$; $c = 30.5013(4)$	$a = b = 4.3860(8)$; $c = 30.5045(6)$	$a = b = 4.3879(7)$; $c = 30.4941(8)$
Volume, Å^3	508.351	508.320	508.215	508.481
Phase Fraction%	95	94.8	96.6	95.5
Distance of bonding, Å				
Bi-Te_2	3.06565(0)	3.07523(0)	3.10172(0)	3.08511(0)
Bi-Te_1	3.25335(0)	3.24817(0)	3.23353(0)	3.24231(0)
Te_2-Te_2	3.65027(0)	3.63765(0)	3.60400(0)	3.62764(0)
Angle of bonding, °				
Bi-Te_2-Bi	94.1041(0)	94.3768(0)	95.0986(0)	94.6227(0)
Te_1-Bi-Te_1	84.7940(0)	84.9497(0)	85.4091(0)	85.1682(0)
Crystallite Size, nm	104.8	97.5	87.8	129.5
Lattice Strain	1.15×10^{-3}	1.33×10^{-3}	1.04×10^{-3}	1.33×10^{-3}
Atomic Position				
Te_1				
x	0	0	0	0
y	0	0	0	0
z	0	0	0	0
Bi				
x	0	0	0	0
y	0	0	0	0
z	0.40028	0.40002	0.39925	0.39969
Te_2				
x	0	0	0	0
y	0	0	0	0
z	0.20976	0.20947	0.20870	0.20924
Ti				
x	…	0	0	0
y	…	0	0	0
z	…	0.40032	0.40065	0.40056

*Standard deviations are given in parentheses and refer to the estimated error in the least significant units.

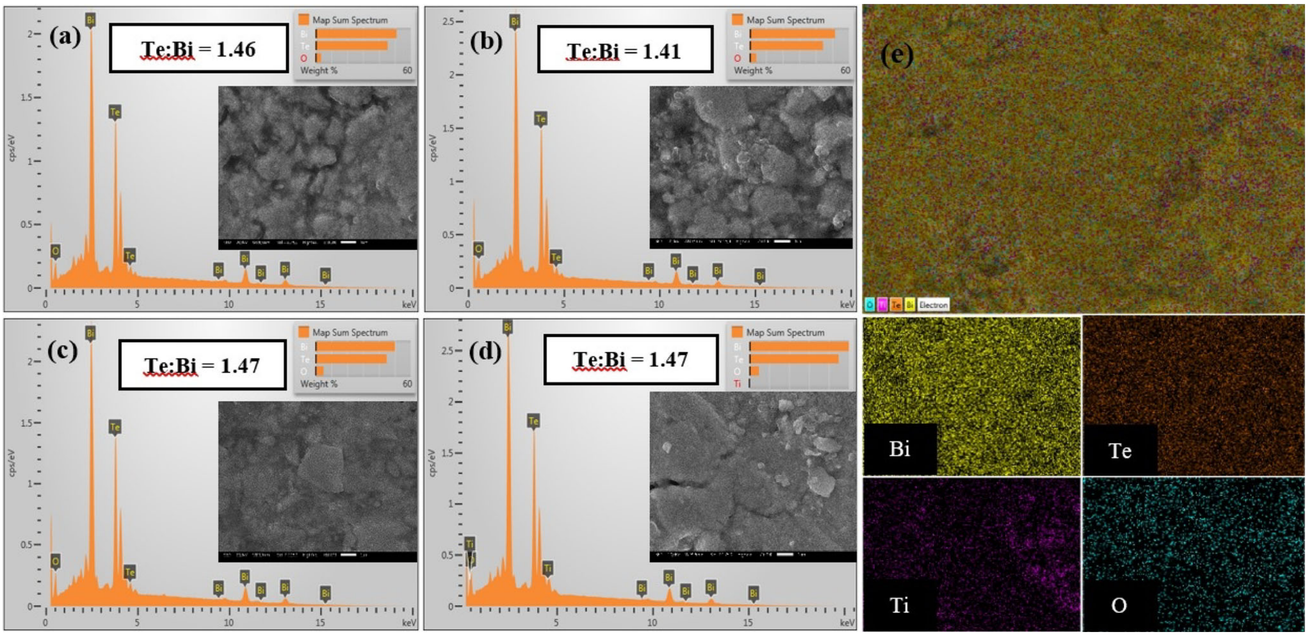

Fig. 2 Scanning electron microscopy with a magnification of 10,000× and the ratio between Bi and Te as a result of energy-dispersive x-ray spectroscopy for (a) Bi_2Te_3, (b) $Bi_{1.95}Ti_{0.05}Te_3$, (c) $Bi_{1.9}$ $Ti_{0.1}Te_3$, (d) $Bi_{1.85}Ti_{0.15}Te_3$, (e) mapping of each constituent element of $Bi_{1.85}Ti_{0.15}Te_3$

highest doping level, while in the other doping variations, it was not. This absence might occur because the doping amount was very small. As shown in Fig. 2(e), Bi and Te are homogeneously distributed, while Ti tends to agglomerate. Ti is probably a residual element that cannot be substituted into Bi sites so it is present in the interstitial spaces in the crystal structure of Bi_2Te_3. Figure 3(a-g) shows some of the results of the thermoelectric property measurements of all samples with Ti doping. Each quantity was measured several times to obtain the standard deviation value.

Figure 3(a) shows that the resistivity increases with increasing temperature, according to which all the samples exhibit metallic behavior. Undoped samples displayed a different trend, especially at temperatures of ~ 445 K. The decrease in the ρ value when a sample is heated indicates the semiconductor state (Ref 49). The ρ value of Bi_2Te_3 is affected by the direction of crystal orientation. In the a-b direction, the plane is more conductive than that perpendicular to the cleavage plane (c-direction) (Ref 16). Increasing Ti doping causes an increase in the ρ value. It can be concluded from the theory proposed by Drašar et al for the Sb_2Te_3 system that if the Ti atom completely substitutes for Bi sites, electron donors are formed, which causes a decrease in the concentration of charge carriers (n) (Ref 31). This is due to the difference in oxidation numbers between Bi and Ti. The defect notation can be written as follows: $2Ti \xrightarrow{Bi_2Te_3} 2Ti^{\cdot}_{Bi}$. A decrease in the concentration of n causes an increase in the ρ value (Ref 2) as in the following equation:

$$\rho = \frac{1}{ne\mu} \quad \text{(Eq 5)}$$

Another possible reason is that the addition of Ti also reduces the mobility (μ) of charge carriers. The ρ value of the undoped sample obtained in this study is greater than that in a previous report (Ref 30). This is due to the presence of an impurity phase consisting of Bi_2TeO_5, which is an insulator (Ref 43, 50).

Figure 3(b) shows the absolute Seebeck coefficient (S) as a function of temperature (T). The S value of all samples increases as a function of increasing temperature, which corresponds to the following equation:

$$S = \frac{8\pi^2 k_B^2}{3eh^2} m^* T \left(\frac{\pi}{3n}\right)^{\frac{2}{3}} (1 + R) \quad \text{(Eq 6)}$$

where k_B is the Boltzmann constant, h is the Planck constant, m^* is the effective mass of the charge carriers, n is the carrier concentration, T is the absolute temperature, and R is the scattering function (Ref 51). The S value was negative, indicating that the majority of charge carriers were electrons. The undoped sample has the greatest absolute S and tends to

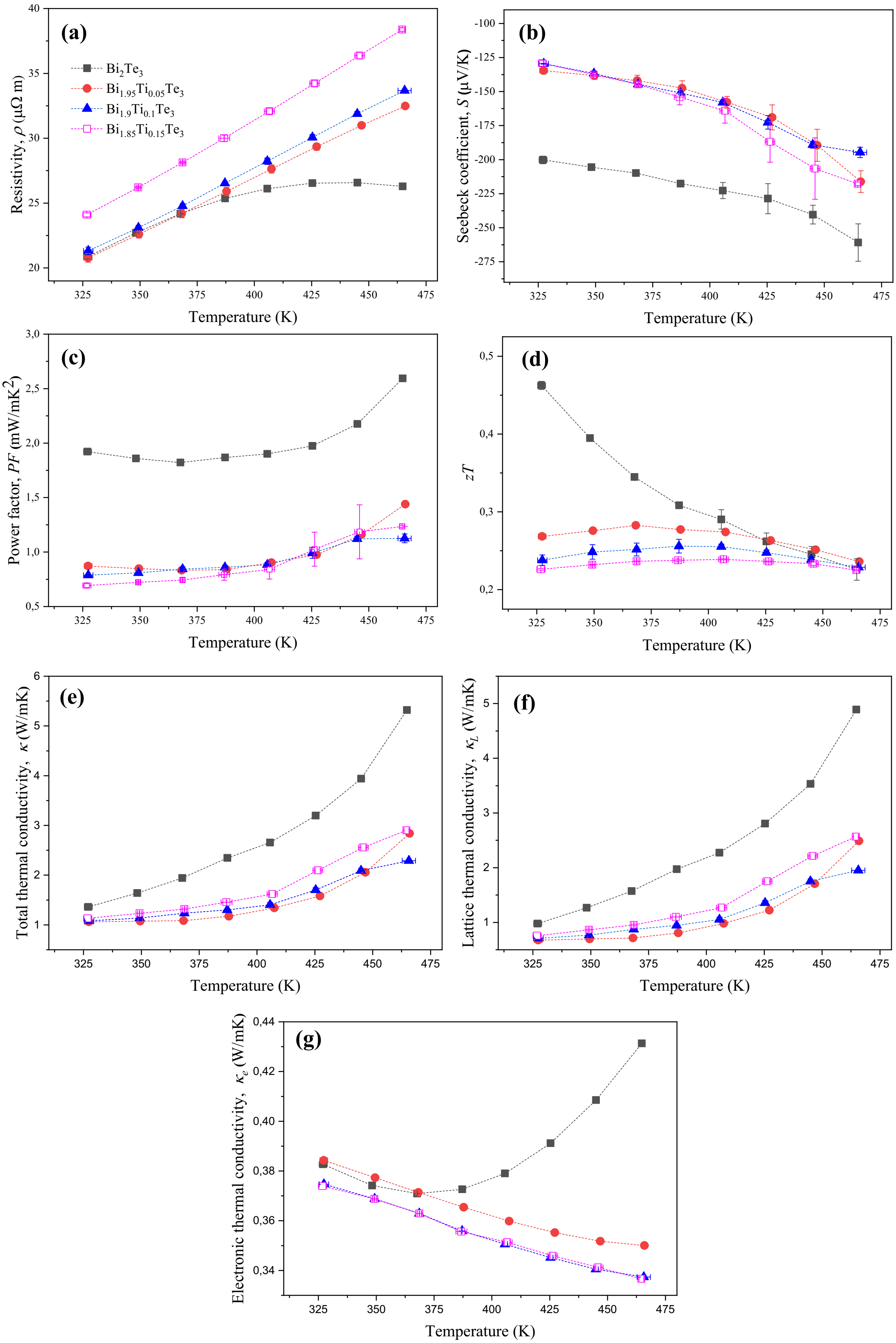

Fig. 3 Temperature dependence of transport measurements for the thermoelectric properties of $Bi_{(2-x)}Ti_xTe_3$ with various amounts of dopant (x = 0, 0.05, 0.1, 0.15) (a) resistivity, ρ, (b) Seebeck coefficient, S, (c) power factor, PF, (d) figure of merit, zT, (e) total thermal conductivity, κ_{tot}, (f) lattice thermal conductivity (κ_1), and (g) electronic thermal conductivity κ_e

Table 2 Figure of merit (zT) of some samples in this research and previous reports

Samples	zT	Temperature, K	Reference
Bi_2Te_3	0.46	327	This work
$Bi_{1.95}$ $Ti_{0.05}$ Te_3	0.27	327	This work
$Bi_{1.9}$ $Ti_{0.1}$ Te_3	0.24	327	This work
$Bi_{1.85}$ $Ti_{0.15}$ Te_3	0.23	327	This work
Bi_2Te_3	0.23	323	(Ref 19)
Bi_2Te_3	0.41	323	(Ref 26)
Bi_2Te_3	0.245	327	(Ref 60)
Bi_2Te_3	0.107	327	(Ref 61)
$Cu_{0.01}Bi_{1.98}5Y_{0.015}Te_{2.7}Se_{0.3}$	~ 1.2	347	(Ref 62)
$Bi_{1.8}Sb_{0.2}Te_{2.7}Se_{0.3}$ + 15 wt.% Te	~ 1.4	425	(Ref 63)

decrease with the addition of Ti. At a temperature of ~ 323 K, the S value of the undoped sample is ~ 200 μV/K. The absolute coefficient Seebeck obtained is greater than that reported in the research conducted by Cao et al. and Wu et al. but slightly smaller than that reported by Chen et al. (Ref 25, 27, 52). Figure 3(c) shows the value of the power factor (PF) resulting from the square of the absolute S divided by ρ. Bi_2Te_3 has the greatest PF value at all measurement points compared to the other samples. This is because the absolute S contributes more than ρ.

The measurement of zT, which is a dimensionless quantity, is carried out using the Harman method, as shown in Fig. 3(d). The largest zT value is observed for the undoped sample at a temperature of approximately 327 K, which is ~ 0.46 and decreases with increasing temperature. This value is similar to that in previous research, which is 0.41 at a temperature of 323 K (Ref 26). Ti doping causes a drastic decrease in zT and a shift in the highest value toward a high temperature. Doping of x = 0.05, 0.1, and 0.15 showed the best results of 0.28 (368 K), 0.26 (387 K), and 0.24 (406 K), respectively.

The value of total thermal conductivity (κ) was obtained based on calculations with measured *zT*, absolute *S*, and ρ values. As shown in Fig. 3(e), Ti doping causes a decrease in the κ value, which is the same result reported by Drašar *et al* for single-crystal Sb_2Te_3 (Ref 31). Figure 3(f) and (g) illustrates that the contribution of lattice thermal conductivity (κ_l) was greater than the factor of charge carriers (κ_e) in Bi_2Te_3. A similar result was reported by Byun et al., who found that the thermal conductivity of the lattice (κ_l) increases as a function of temperature (Ref 23). The κ_e value shows a different trend for pristine and Ti-doped samples.

The band structure and partial density of states (PDOS) of Bi_2Te_3 without SOC calculation are shown in Fig. 4(a). The calculated direct band gap is approximately 0.37 eV in Γ momentum space. Meanwhile, the calculation with SOC is shown in Fig. 4(b), where the indirect band gap is approximately 0.14 eV between Γ and M momentum space. This value is similar to several previous reports of 0.154 eV (Ref 53) and 0.13 eV (Ref 18). The calculation of the PDOS with SOC showed that the state of the Te atom dominated in the valence band and passed the Fermi level, which indicated that Bi_2Te_3 is metallic. The energy gap of $Bi_{(2-x)}Ti_xTe_3$ was measured using UV–Vis spectrophotometry. The data are displayed for the wavelength region in which the sample absorbs light. The absorption data obtained are plotted in $(\alpha d)^2$ as a function of $E = \frac{hc}{e\lambda}$ The intercept of the slope on the X-axis is the energy gap (Eg) value.

Figure 5(a-d) shows that the Eg value tends to increase with increasing Ti doping. These results are certainly consistent with the ρ data, which increase with Ti doping. According to the experimental results, all materials have high Eg, with values ranging from 3.07 to 3.9 eV, because the nanoscale crystallite size increases dislocation density (Ref 54, 55, 56) and Ti doping in $Bi_{(2-x)}Ti_xTe_3$ compounds increases the difference in electronegativity between Ti^{4+} and Bi^{3+} as cations with Te^{2-} as anions (Ref 57, 58).

Figure 6(a) shows the results of hardness measurements, which were conducted several times in 5 different areas. The sample hardness value increases as a function of dopant

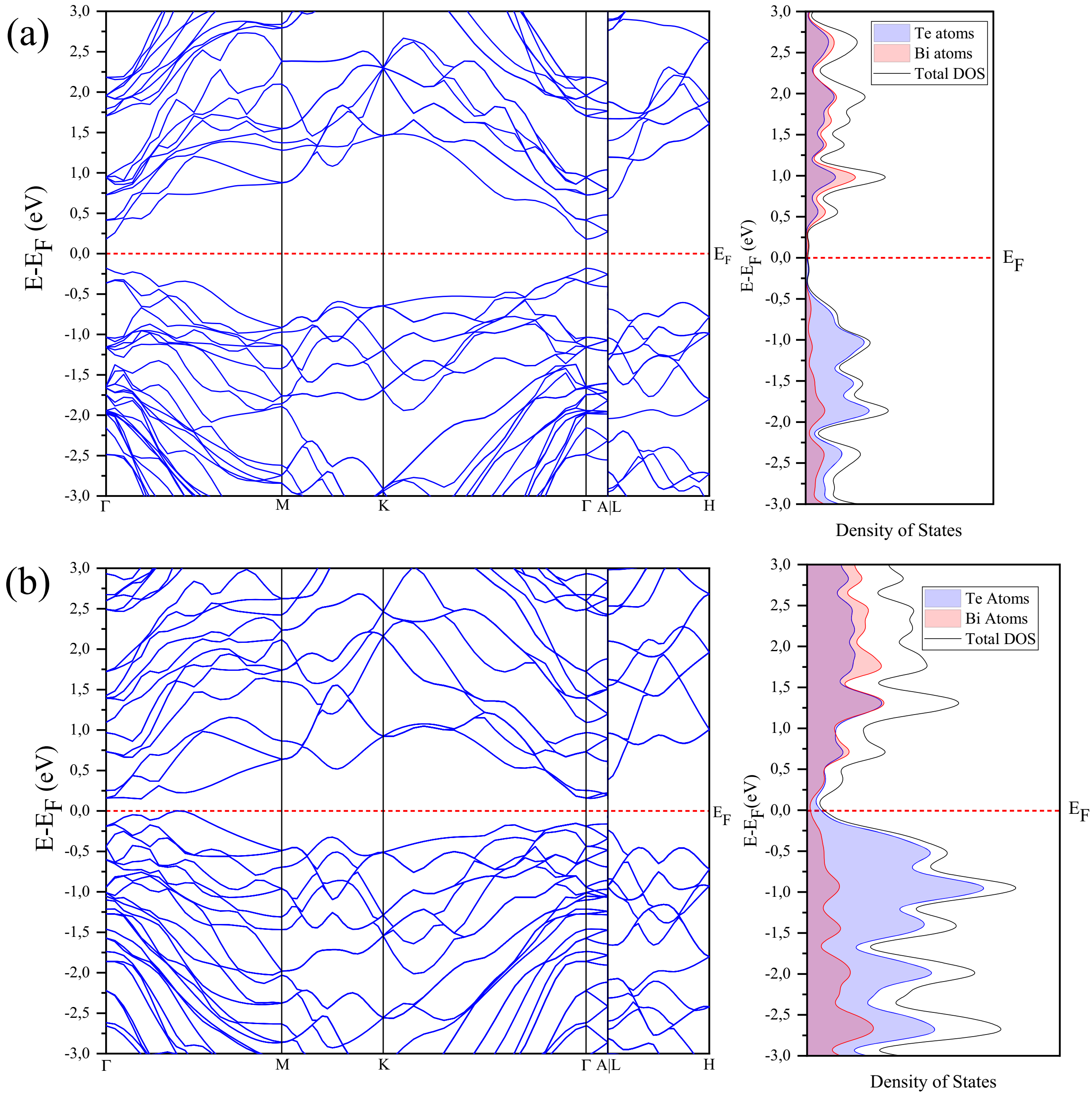

Fig. 4 Band structure and partial density of states (PDOS) of undoped (Bi_2Te_3) (a) without SOC and (b) with SOC

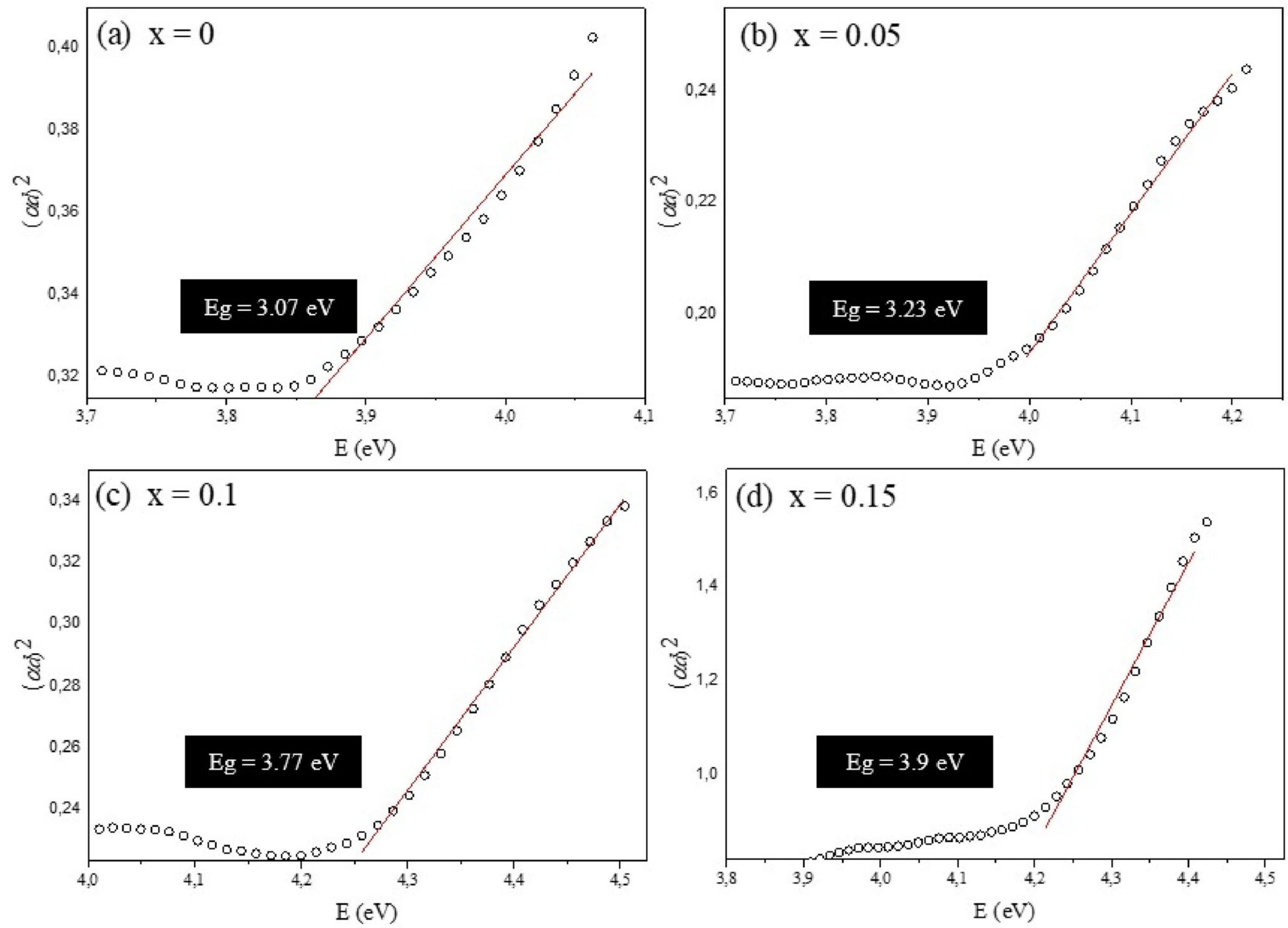

Fig. 5 Band gap energy as a result of UV–Vis spectrophotometry measurements of (a) Bi_2Te_3, (b) $Bi_{1.95}Ti_{0.05}Te_3$, (c) $Bi_{1.9}$ $Ti_{0.1}Te_3$, and (d) $Bi_{1.85}Ti_{0.15}Te_3$

concentration, from 27.14-31.4 VHN. The hardness value is similar to that reported by Kartika et al for the undoped sample, while for the doped sample, it is quite different (Ref 32). This is due to the difference in the calculation method for Ti doping. The corrosion rate of $Bi_{(2-x)}Ti_xTe_3$ was characterized by using a potentiodynamic technique in a 3 wt.% NaCl solution. The inserted graph in Fig. 6(b) shows that Ti doping reduces the corrosion rate of Bi_2Te_3. This is because titanium has excellent chemical stability (Ref 59). Table 2 shows the figure of merit (zT) of our samples in this study and earlier publications (Ref 19, 26, 60–63).

4. Conclusions

We successfully synthesized $Bi_{(2-x)}Ti_xTe_3$ with various doping concentrations (x = 0, 0.05, 0.1, and 0.15) using a solid-state reaction and carbon burial sintering method. The powder x-ray diffraction pattern of all samples revealed the presence of Bi_2TeO_5 impurities, with the greatest amount at x = 0.05, which was 5.2%. The highest figure of merit (zT) was found in the undoped sample, which was 0.46 at 327 K, and tended to decrease with increasing doping concentration. The energy gap for Bi_2Te_3 was 3.07 eV and widened with

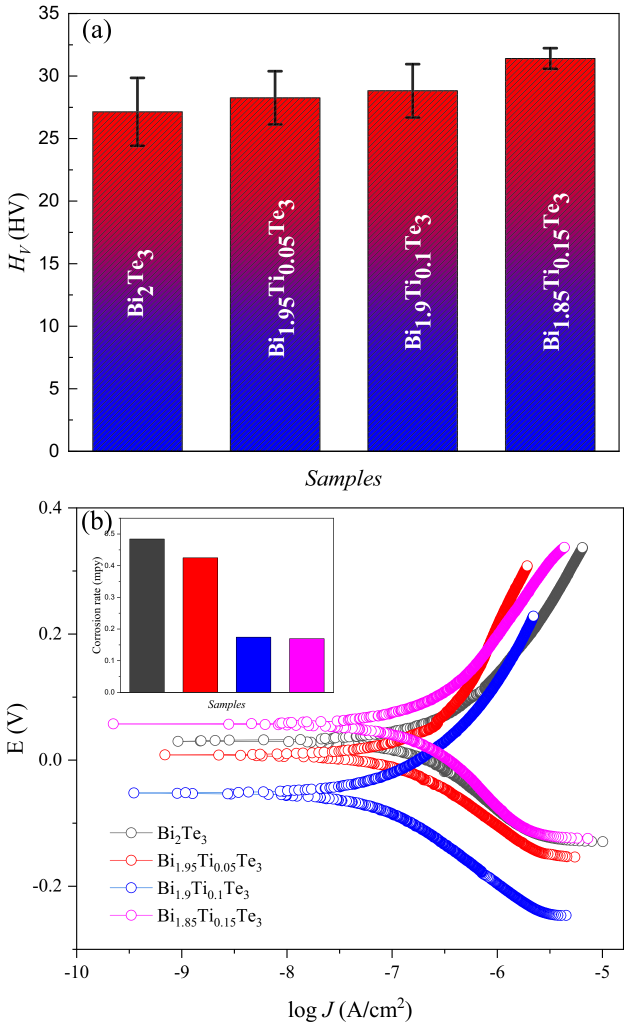

Fig. 6 (a) The hardness measurement results of bulk $Bi_{(2-x)}Ti_xTe_3$ with different amounts of Ti doping and (b) the corrosion rate of $Bi_{(2-x)}Ti_xTe_3$ as a result of potentiodynamic measurements

increasing Ti doping. Ti doping caused an increase in hardness and reduced the corrosion rate.

Acknowledgment

We acknowledge the Research Center for Advanced Materials, National Research and Innovation Agency (BRIN), Department of Metallurgy engineering, Universitas Jenderal Ahmad Yani (UNJANI), and Advanced Characterization Laboratories Bandung, E-Layanan Sains, BRIN, Indonesia for providing several synthesis and characterization facilities.

Conflict of interest

The authors declare no conflict of interest.

References

1. L.E. Bell, Cooling, Heating, Generating Power, and Recovering Waste Heat with Thermoelectric Systems, *Science*, 2008, **321**(5895), p 1457–1461
2. G.J. Snyder and E.S. Toberer, Complex Thermoelectric Materials, *Mater. Renew. Sustain. Energy*, 2010, **7**, p 101–114
3. Y. Hosokawa, K. Tomita, and M. Takashiri, Growth of Single-Crystalline Bi_2Te_3 Hexagonal Nanoplates with and without Single Nanopores during Temperature-Controlled Solvothermal Synthesis, *Sci. Rep.*, 2019, **9**(1), p 10790
4. M. Kashiwagi, S. Hirata, K. Harada, Y. Zheng, K. Miyazaki, M. Yahiro, and C. Adachi, Enhanced Figure of Merit of a Porous Thin Film of Bismuth Antimony Telluride, *Appl. Phys. Lett.*, 2011, **98**(2), p 023114
5. H.-S. Kim, Z.M. Gibbs, Y. Tang, H. Wang, and G.J. Snyder, Characterization of Lorenz Number with Seebeck Coefficient Measurement, *APL Mater.*, 2015, **3**(4), p 041506
6. M.H. Lee, K.-R. Kim, J.-S. Rhyee, S.-D. Park, and G.J. Snyder, High Thermoelectric Figure-of-Merit in Sb_2Te_3/Ag_2Te Bulk Composites as Pb-Free p-Type Thermoelectric Materials, *J. Mater. Chem. C*, 2015, **3**(40), p 10494–10499
7. M.-K. Han, J. Hwang, and S.-J. Kim, Improved Thermoelectric Properties of N-Type Bi2Te3 Alloy Deriving from Two-Phased Heterostructure by the Reduction of CuI with Sn, *J. Mater. Sci.: Mater. Electron*, 2019, **30**(2), p 1282–1291
8. H.-T. Liu, Q. Sun, Y. Zhong, Q. Deng, L. Gan, F.-L. Lv, X.-L. Shi, Z.-G. Chen, and R. Ang, High-Performance in n-Type PbTe-Based Thermoelectric Materials Achieved by Synergistically Dynamic Doping and Energy Filtering, *Nano Energy*, 2022, **91**, 106706
9. P.-C. Dedi, C.-H. Lee, G.-P. Chien, W.-C. Dong, C.-L. Huang, C.-M. Chen, S.R. Tseng, C.-H. LeeHarutyunyan, and Y.-Y. Chen, Stress-Induced Growth of Single-Crystalline Lead Telluride Nanowires and Their Thermoelectric Transport Properties, *Appl. Phys. Lett.*, 2013, **103**(2), 023115
10 B. Dado, Y. Gelbstein, and M.P. Dariel, Nucleation of Nanosize Particles Following the Spinodal Decomposition in the Pseudo-Ternary Ge0.6Sn0.1Pb0.3Te Compound, *Scripta Mater.*, 2010, **62**(2), p 89–92
11. Y. Gelbstein, B. Dado, O. Ben-Yehuda, Y. Sadia, Z. Dashevsky, and M.P. Dariel, High Thermoelectric Figure of Merit and Nanostructuring in Bulk *p*-Type $Ge_x(Sn_yPb_{1-y})_{1-x}Te$ Alloys Following a Spinodal Decomposition Reaction, *Chem. Mater.*, 2010, **22**(3), p 1054–1058
12. B. Jiang, W. Wang, S. Liu, Y. Wang, C. Wang, Y. Chen, L. Xie, M. Huang, and J. He, High Figure-of-Merit and Power Generation in High-Entropy GeTe-Based Thermoelectrics, *Science*, 2022, **377**(6602), p 208–213
13. Z. Li, Y. Chen, J.-F. Li, H. Chen, L. Wang, S. Zheng, and G. Lu, Systhesizing SnTe Nanocrystals Leading to Thermoelectric Performance Enhancement via an Ultra-Fast Microwave Hydrothermal Method, *Nano Energy*, 2016, **28**, p 78–86
14. Y. Sadia, M. Elegrably, O. Ben-Nun, Y. Marciano, and Y. Gelbstein, Submicron Features in Higher Manganese Silicide, *J. Nanomater.*, 2013, **2013**, p 1–5
15. B. Poudel, Q. Hao, Y. Ma, Y. Lan, A. Minnich, B. Yu, X. Yan, D. Wang, A. Muto, D. Vashaee, X. Chen, J. Liu, M.S. Dresselhaus, G. Chen, and Z. Ren, High-Thermoelectric Performance of Nanostructured Bismuth Antimony Telluride Bulk Alloys, *Science*, 2008, **320**(5876), p 634–638
16. H.J. Goldsmid, Introduction to Thermoelectricity, 1st ed., R. Hull, R. M. Osgood, Jr., J. Parisi, H. Warlimont, Springer, 2009, p 79–80
17. B.K. Gupta, R. Sultana, S. Singh, V. Singh, G. Awana, A. Gupta, B. Singh, A.K. Srivastava, O.N. Srivastava, S. Auluck, and V.P.S. Awana, Unexplored Photoluminescence from Bulk and Mechanically Exfoliated Few Layers of Bi_2Te_3, *Sci. Rep.*, 2018, **8**(1), p 9205
18. A. Lawal and A. Shaari, Density Functional Theory Study of Electronic Properties of Bi_2Se_3 and Bi_2Te_3, *Mal. J. Fund. Appl. Sci.*, 2017, **12**(3), p 99–101
19. Q. Zhang, X. Ai, L. Wang, Y. Chang, W. Luo, W. Jiang, and L. Chen, Improved Thermoelectric Performance of Silver Nanoparticles-Dispersed Bi_2Te_3 Composites Deriving from Hierarchical Two-Phased Heterostructure, *Adv. Funct. Mater.*, 2015, **25**(6), p 966–976
20. Z.J. Vafa and M.M.B. Mohagheghi, Synthesis of High Purity Bismuth Telluride (Bi_2Te_3) Nanostructures by Co-Precipitation Process and Annealing under Hydrazine Vapor: Structural and Thermoelectric Studies, *J. Electron. Mater.*, 2021, **50**(9), p 5268–5281
21. I. Malik, T. Srivastava, K.K. Surthi, C. Gayner, and K.K. Kar, Enhanced Thermoelectric Performance of N-Type Bi_2Te_3 Alloyed with Low Cost and Highly Abundant Sulfur, *Mater. Chem. Phys.*, 2020, **255**, 123598

22. S. Irfan, J. Luo, F. Ping, and Z. Zhuanghao, Theoretical and Experimental Investigation of Magnetic Properties of Iodine and Cerium Co-Doped Bi_2Te_3 Nanoparticles, *J. Mater. Res. Technol.*, 2020, **9**(6), p 13893–13901
23. S. Byun, J. Cha, C. Zhou, Y.K. Lee, H. Lee, S.H. Park, W.B. Lee, and I. Chung, Unusual N-Type Thermoelectric Properties of Bi_2Te_3 Doped with Divalent Alkali Earth Metals, *J. Solid State Chem.*, 2019, **269**, p 396–400
24. M. Yaprintsev, R. Lyubushkin, O. Soklakova, and O. Ivanov, Effects of Lu and Tm Doping on Thermoelectric Properties of Bi_2Te_3 Compound, *J. Electron. Mater.*, 2018, **47**(2), p 1362–1370
25. R. Cao, Z. Zhu, X.-J. Li, X. Hu, and H. Song, Enhanced Thermoelectric Properties of the Lu-Doped and CNT-Dispersed Bi_2Te_3 Alloy, *Appl. Phys. A*, 2019, **125**(2), p 126
26. T. KristiantoroDedi and V. Fauzia, The Influence of Dy Concentration on the Thermoelectric Properties of N-Type Dy-Doped Bi_2Te_3 Pellets Prepared by Hydrothermal and Carbon Burial Sintering, *J. Phys. Chem. Solids*, 2021, **158**, p 110241
27. F. Wu, H. Song, J. Jia, and X. Hu, Effects of Ce, Y, and Sm Doping on the Thermoelectric Properties of Bi_2Te_3 Alloy, *Prog. Nat. Sci.: Mater. Int.*, 2013, **23**(4), p 408–412
28. A. Soni, Z. Yanyuan, Y. Ligen, M.K.K. Aik, M.S. Dresselhaus, and Q. Xiong, Enhanced Thermoelectric Properties of Solution Grown $Bi_2Te_{3-x}Se_x$ Nanoplatelet Composites, *Nano Lett.*, 2012, **12**(3), p 1203–1209
29. S. Liu, N. Peng, Y. Bai, D. Ma, F. Ma, and K. Xu, Fabrication of Cu-Doped Bi_2Te_3 Nanoplates and Their Thermoelectric Properties, *J. Electron. Mater.*, 2017, **46**(5), p 2697–2704
30. K.T. Kim, S.Y. Choi, E.H. Shin, K.S. Moon, H.Y. Koo, G.-G. Lee, and G.H. Ha, The Influence of CNTs on the Thermoelectric Properties of a CNT/Bi_2Te_3 Composite, *Carbon*, 2013, **52**, p 541–549
31. Č Drašar, M. Steinhart, P. Lošťák, H.-K. Shin, J.S. Dyck, and C. Uher, Transport Coefficients of Titanium-Doped Sb_2Te_3 Single Crystals, *J. Solid State Chem.*, 2005, **178**(4), p 1301–1307
32. N.L. Kartika, A. Septiani, M.P. Rosha, T. Kristiantoro, A.R. Nugraha, R.H. Mulyani, and Dedi, Thermoelectric Properties of Ti Doping in Bismuth Telluride Prepared by Powder Metallurgy Process, *2021 International Conference on Radar, Antenna, Microwave, Electronics, and Telecommunications (ICRAMET)*, (Bandung, Indonesia), IEEE, 2021, p 21–26
33. D. Liu, Y. Zhang, H. Kang, J. Li, Z. Chen, and T. Wang, Direct Preparation of La-Doped $SrTiO_3$ Thermoelectric Materials by Mechanical Alloying with Carbon Burial Sintering, *J. Eur. Ceram. Soc.*, 2018, **38**(2), p 807–811
34. B.H. Toby and R.B. Von Dreele, GSAS-II: The Genesis of a Modern Open-Source All Purpose Crystallography Software Package, *J. Appl. Crystallogr.*, 2013, **46**(2), p 544–549
35. T.C. Harman, Special Techniques for Measurement of Thermoelectric Properties, *J. Appl. Phys.*, 1958, **29**(9), p 1373–1374
36. H. Kohri and T. Yagasaki, Corrosion Behavior of Bi_2Te_3-Based Thermoelectric Materials Fabricated by Melting Method, *J. Electron. Mater.*, 2017, **46**(5), p 2587–2592
37. P. Giannozzi, O. Andreussi, T. Brumme, O. Bunau, M. BuongiornoNardelli, M. Calandra, R. Car, C. Cavazzoni, D. Ceresoli, M. Cococcioni, N. Colonna, I. Carnimeo, A. Dal Corso, S. De Gironcoli, P. Delugas, R.A. DiStasio, A. Ferretti, A. Floris, G. Fratesi, G. Fugallo, R. Gebauer, U. Gerstmann, F. Giustino, T. Gorni, J. Jia, M. Kawamura, H.-Y. Ko, A. Kokalj, E. Küçükbenli, M. Lazzeri et al., Advanced Capabilities for Materials Modelling with Quantum ESPRESSO, *J. Phys. Condens. Matter*, 2017, **29**(46), p 465901
38. P. Giannozzi, S. Baroni, N. Bonini, M. Calandra, R. Car, C. Cavazzoni, D. Ceresoli, G.L. Chiarotti, M. Cococcioni, I. Dabo, A. Dal Corso, S. De Gironcoli, S. Fabris, G. Fratesi, R. Gebauer, U. Gerstmann, C. Gougoussis, A. Kokalj, M. Lazzeri, L. Martin-Samos, N. Marzari, F. Mauri, R. Mazzarello, S. Paolini, A. Pasquarello, L. Paulatto, C. Sbraccia, S. Scandolo, G. Sclauzero, A.P. Seitsonen et al., QUANTUM ESPRESSO: A Modular and Open-Source Software Project for Quantum Simulations of Materials, *J. Phys. Condens. Matter.*, 2009, **21**(39), p 395502
39. J.P. Perdew, K. Burke, and M. Ernzerhof, Generalized Gradient Approximation Made Simple, *Phys. Rev. Lett.*, 1996, **77**(18), p 3865–3868
40. J.P. Perdew, A. Ruzsinszky, G.I. Csonka, O.A. Vydrov, G.E. Scuseria, L.A. Constantin, X. Zhou, and K. Burke, Restoring the Density-Gradient Expansion for Exchange in Solids and Surfaces, *Phys. Rev. Lett.*, 2008, **100**(13), p 136406
41. W. Kohn and L.J. Sham, Self-Consistent Equations Including Exchange and Correlation Effects, *Phys. Rev.*, 1965, **140**(4A), p A1133–A1138
42 P.E. Blochl, Projector Augmented-Wave Method, *Phys. Rev. B*, 1994, **50**, p 17953
43. Y. Du, K.F. Cai, H. Li, and B.J. An, The Influence of Sintering Temperature on the Microstructure and Thermoelectric Properties of N-Type $Bi_2Te_{3-x}Se_x$ Nanomaterials, *J. Electron. Mater.*, 2011, **40**(5), p 518–522
44. H. Shao, X. Bai, H. Cui, G. Pan, P. Jing, S. Qu, J. Zhu, Y. Zhai, B. Dong, and H. Song, White Light Emission in Bi^{3+}/Mn^{2+} Ion Co-Doped $CsPbCl_3$ Perovskite Nanocrystals, *Nanoscale*, 2018, **10**(3), p 1023–1029
45. Z. Wang, Y. Li, H. Chen, J. Fan, X. Wang, and X. Ma, Correlation between the Radius of Acceptor Ion and the Dielectric Properties of Co-Doped TiO_2 Ceramics, *Ceram. Int.*, 2019, **45**(12), p 14625–14633
46. C. Kulsi, M. Mitra, K. Kargupta, and D. Banerjee, Thermoelectric Properties of Nanostructured Bismuth Telluride (Bi_2Te_3) with Annealing Time and Its Composite with Reduced Graphene Oxide (RGO), *J. Mater. Sci. Mater. Electron.*, 2019, **30**(2), p 1850–1860
47. H. Cho, S.Y. Back, J.H. Kim, O. Inturu, H.S. Lee, and J.-S. Rhyee, Enhancement of Thermoelectric Properties over a Wide Temperature Range by Lattice Disorder and Chemical Potential Tuning in a $(CuI)_y(Bi_2Te_3)_{0.95-x}(Bi_2Se_3)_x(Bi_2S_3)_{0.05}$ Quaternary System, *RSC Adv.*, 2019, **9**(8), p 4190–4197
48 V. Mote, Y. Purushotham, and B. Dole, Williamson-Hall Analysis in Estimation of Lattice Strain in Nanometer-Sized ZnO Particles, *J. Theor. Appl. Phys.*, 2012, **6**(1), p 6
49. I. Bolshakova, F.S. Terra, G.M. Mahmoud, and A.M. Mansour, High Quality InSb Microcrystal Hall Sensor Doped with Te or Bi, *Int. J. Adv. Appl. Phys. Res.*, 2016, **3**, p 5–10
50. E. Hartmann, Electrical Conductivity of Bi_2TeO_5 Single Crystals at High Temperatures, *Cryst. Res. Technol.*, 2001, **36**(8–10), p 911–916
51. K. Singkaselit, A. Sakulkalavek, and R. Sakdanuphab, Effects of Annealing Temperature on the Structural, Mechanical and Electrical Properties of Flexible Bismuth Telluride Thin Films Prepared by High-Pressure RF Magnetron Sputtering, *Adv. Nat. Sci.: Nanosci. Nanotechnol.*, 2017, **8**(3), p 035002
52. L. Chen, D. Mei, Y. Wang, and Y. Li, Ni Barrier in Bi_2Te_3-Based Thermoelectric Modules for Reduced Contact Resistance and Enhanced Power Generation Properties, *J. Alloy. Compd.*, 2019, **796**, p 314–320
53 M. Kim, A.J. Freeman, and C.B. Geller, Screened Exchange LDA Determination of the Ground and Excited State Properties of Thermoelectrics: Bi_2Te_3, *Phys. Rev. B*, 2005, **72**(3), p 035205
54. S.M. Elahi, A. Taghizadeh, A. Hadizadeh, and L. Dejam, Effect of Thickness and Annealing on Structural and Optical Properties of Bi_2Te_3 Thin Films Prepared from Bi_2Te_3 Nanoparticels, *Int. J. Thin Film Sci. Technol.*, 2014, **3**(1), p 13–18
55 S. Subramanian and D.P. Padiyan, Effect of Structural, Electrical and Optical Properties of Electrodeposited Bismuth Selenide Thin Films in Polyaniline Aqueous Medium, *Mat. Chem. Phys.*, 2008, **107**, p 392–398
56. H.F. Matare, *Defect Electronics in semiconductors*, Wiley, New York, Springer, 1971
57. W.G. Zeier, A. Zevalkink, Z.M. Gibbs, G. Hautier, M.G. Kanatzidis, and G.J. Snyder, Thinking Like a Chemist: Intuition in Thermoelectric Materials, *Angew. Chem. Int. Ed.*, 2016, **55**(24), p 6826–6841
58. W. Liu, Z. Han, J. Ji, T. Feng, J. Yang, and W. Zhang, Uplimit (ZT)Max and Effective Merit Parameter B* of Thermoelectric Semiconductors, *Mater. Today Phys.*, 2023, **31**, 100989
59. M. Nakagawa and S. Matsuya, Shiraishi, and Ohta M, Effect of Fluoride Concentration and pH on Corrosion Behaviour of Titanium for Dental Use, *J. Dent. Res.*, 1999, **78**(9), p 1568–1572
60. S. Kumar, D. Chaudhary, and N. Khare, Enhanced Thermoelectric Figure of Merit in Bi_2Te_3–CNT–PEDOT Nanocomposite by Introducing Conducting Interfaces in Bi_2Te_3 Nanostructures, *APL Mater.*, 2019, **7**(8), p 081123
61. K. Ahmad, C. Wan, M.A. Al-Eshaikh, and A.N. Kadachi, Enhanced Thermoelectric Performance of Bi_2Te_3 Based Graphene Nanocomposites, *Appl. Surf. Sci.*, 2019, **474**, p 2–8

62 H. Lee, T. Kim, S.C. Son, J. Kim, D. Kim, J. Lee, and I. Chung, Unique Microstructures and High Thermoelectric Performance in n–Type $Bi_2Te_{2.7}Se_{0.3}$ by the Dual Incorporation of Cu and Y, *Mater. Today Phys.*, 2023, **31**, p 100986
63. B. Zhu, X. Liu, Q. Wang, Y. Qiu, Z. Shu, Z. Guo, Y. Tong, J. Cui, M. Gu, and J. He, Realizing Record High Performance in n-type Bi_2Te_3-Based Thermoelectric Materials, *Energy Environ. Sci.*, 2020, **13**, p 2106–2114